Geophysical Research Letters

Supporting Information for

Meltwater Penetration Through Temperate Ice Layers in the Percolation Zone at DYE-2, Greenland Ice Sheet

Samimi, S.[1], S.J. Marshall[1,2] and M. MacFerrin[3]

[1] Department of Geography, University of Calgary, Calgary, Alberta, Canada
[2] Environment and Climate Change Canada, Gatineau, Quebec, Canada
[3] Cooperative Institute for Research in Environmental Sciences, University of Colorado, Boulder, CO, USA

Contents of this file

Additional Supporting Information (Files uploaded separately)

Introduction

Details of the firn thermistor, time-domain reflectometry (TDR), and automatic weather station (AWS) data from summer 2016 are included here. Figure S1 shows the location of the study, at DYE-2 in southwestern Greenland, along with our two firn pits, referred to as Sites A and B. Figure S2 plots the measured air temperature and snow surface height/snow depth data, along with the calculated surface energy balance and melt at the AWS site. Figure S3 illustrates the full evolution of the air, snow, and firn temperatures and the dielectric permittivities at Site A through summer 2016. We also provide details of the surface energy balance and subsurface thermal/hydrological model, and Figure S4 presents model results for the subsurface temperature evolution and the energy fluxes associated with refreezing and meltwater advection.

Data from this study are being archived at the University of Calgary data repository, and are also provided with the Supporting Information as Excel files. This is directly from the datalogger download, without processing, but missing or off-scale data values (-99999) have been replaced by either NaN or an empty cell.

Text S1

Figure S1 shows the location of the study in southwestern Greenland, including our two firn pits (sites A and B). Co-ordinates of each firn pit are included in Table S1, along with details of the initial snow temperature, density, dielectric permittivity, and sensor installation depths.

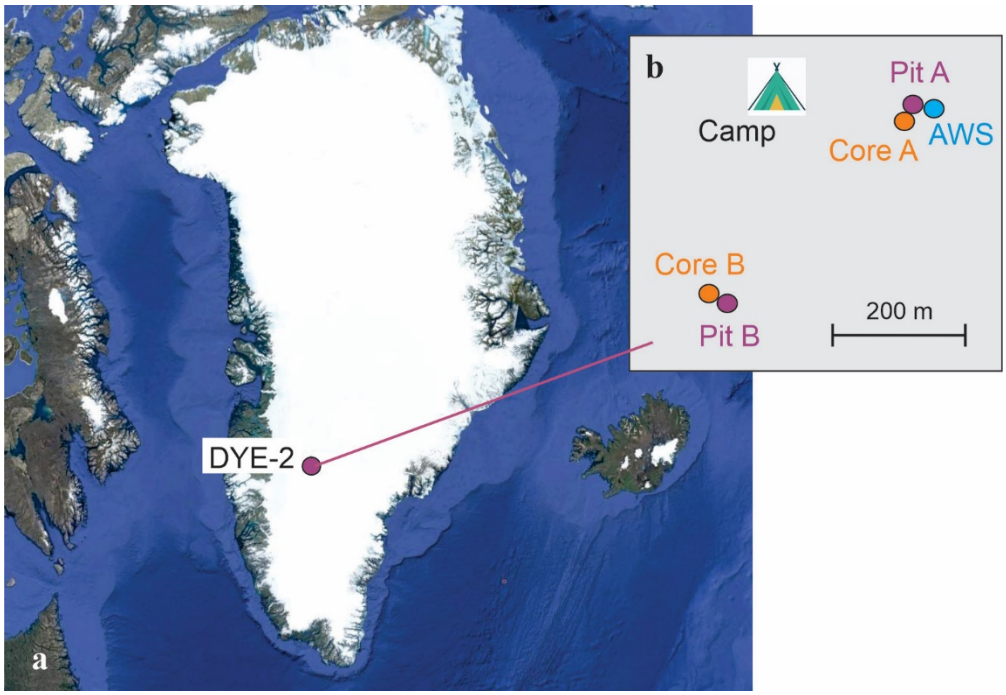

Figure S1. Study site at DYE-2, southwestern Greenland. AWS refers to the automatic weather station. Firn pits A and B were 402 m apart. Image (a) courtesy of Google Earth.

An automatic weather station (AWS) was set up on a tripod adjacent to firn pit A. The AWS was configured to measure air temperature, relative humidity, air pressure, incoming and outgoing shortwave and longwave radiation (Kipp and Zonen CNR1 radiometer), wind speed and direction, and snow surface height, based on an SR50A ultrasonic depth sounder. The SR50A sensor was installed separately on a pole drilled into the firn, in order to maintain a fixed height while the snow surface changed. Air

temperature, relative humidity, and snow surface height were also measured at firn pit B. All sensors were wired to CR1000 Campbell Scientific dataloggers at each site and were programmed to record 30-minute averages of 10-second measurements.

The AWS was installed on April 28, 2016 and was left in place until spring 2017, when we returned to the site to collect data and take the station down. Data were recorded continuously from the time of installation until November 2016, at which point the battery weakened due to insufficient solar charging. There are no data gaps in the AWS record from April 28 through October 28, 2016. This study focuses on the meteorological conditions and surface energy balance from May to September, 2016, covering the complete 2016 melt season.

	Site A (installed 16/05/11) 66.47775°N, 46.28510°W				Site B (installed 16/05/08) 66.47505°N, 46.29115°W			
Level	d (m)	T_{s0} (°C)	ε_{b0}	ρ_0 (kg m^{-3})	d (m)	T_{s0} (°C)	ε_{b0}	ρ_0 (kg m^{-3})
1	0.3	–7.3	2.37	380	0.1	–3.7	2.31	280
2	0.6	–10.1	1.88	380	0.2	–4.2	2.49	310
3	0.9	–12.7	2.21	230	0.4	–6.6	2.09	280
4	1.4	–14.5	2.32	510	0.6	–9.2	2.06	320
5	1.8	–15.1	2.37	410	0.9	–11.9	2.47	640
6	2.1	–15.6	2.44	460	1.2	–13.1	2.54	620
7	2.8	–15.7	2.14	360	1.5	–14.4	2.65	560
8	3.7	–15.8	2.67	520	1.6	–14.9	2.36	480

Table S1. Installation depths (d) and initial snow/firn temperature (T_0), bulk dielectric permittivity (ε_{b0}), and density (ρ_0) at each measurement level for sites A and B.

Surface Energy Balance Model

The surface energy balance was calculated following the model of Ebrahimi and Marshall (2016), including a subsurface model for heat conduction in the upper 10 m of firn and snow, the approximate depth of penetration of the annual temperature wave (Cuffey and Paterson, 2010). Net energy at the ice sheet surface is a function of the energy fluxes at the surface-atmosphere interface,

$$Q_N = Q_S^{\downarrow}(1-\alpha) + Q_L^{\downarrow} - Q_L^{\uparrow} + Q_H + Q_E + Q_C\,, \quad (1)$$

where $Q_S^{\downarrow}$ is the incoming shortwave radiation, α is the surface albedo, $Q_L^{\downarrow}$ and $Q_L^{\uparrow}$ are the incoming and outgoing longwave radiation, Q_H and Q_E are the sensible and latent heat fluxes, and Qc is the upward-directed conductive heat flux from the snow/firn to the

surface. All energy fluxes have units W m^{-2} and are defined to be positive when they are sources of energy to the surface. Energy fluxes associated with precipitation are assumed to be negligible.

When the surface temperature is below 0°C, net energy Q_N goes to heating or cooling the surface layer of the snow/firn, a 0.1-m layer within the subsurface model. If the surface is at 0°C and $Q_N > 0$, net energy goes to melting, following

$$\dot{m} = Q_N/(\rho_w L_f)\,, \tag{2}$$

where $\dot{m}$ is the melt rate (m s^{-1}), and L_f is the latent heat of fusion. If net energy is negative, any liquid water that is present will refreeze and then the surface layer will cool.

To calculate net energy in Eq. (1), radiation fluxes were directly measured and the turbulent fluxes were modelled using a bulk aerodynamic approach (e.g., Andreas, 2002),

$$Q_H = \rho_a c_p k^2 v \left[\frac{T_a(z)-T_s}{\ln(z/z_0)\ln(z/z_{0H})}\right], \tag{3}$$

and

$$Q_E = \rho_a L_v k^2 v \left[\frac{q_a(z)-q_s}{\ln(z/z_0)\ln(z/z_{0E})}\right]. \tag{4}$$

Here T_a, q_a and v are the air temperature, specific humidity, and wind speed measured at the AWS, T_s and q_s are the temperature and specific humidity at the snow surface, ρ_a is the air density, c_p is the specific heat capacity of air, L_v is the latent heat of evaporation, and k = 0.4 is von Karman's constant. Parameters z_0, z_{0H}, and z_{0E} refer to the roughness length scales for turbulent exchange of momentum, heat, and moisture. We adopt fixed roughness values based on typical values for snow-covered glaciers (Brock et al., 2006), z_0 = 1 mm and $z_{0H} = z_{0E} = z_0/100$. We estimate the surface skin temperature T_s from an inversion of Stefan-Boltzmann's equation, using measurements of outgoing longwave radiation. The surface humidity q_s can then be calculated from the saturation specific humidity over snow at temperature T_s.

Conductive heat flux to the ice sheet surface, Q_C, is calculated from the vertical heat conduction in the upper three layers of the subsurface model (described in more detail below), based on a three-point forward finite difference:

$$Q_C = -\frac{k_t}{2\Delta z}(3T_1 - 4T_2 + T_3). \tag{5}$$

for thermal conductivity k_t and layer thickness Δz. The surface energy balance is calculated every 30 minutes based on the AWS data, Eqs. (3)-(5), and the subsurface temperature model, giving an estimate of 30-minute melt amounts over summer 2016.

Subsurface Temperature Model

The subsurface model includes a simple one-dimensional treatment of the coupled thermodynamic and hydrological evolution in the upper 10 m of snow and firn, including a simple treatment of meltwater percolation and refreezing (Samimi and Marshall, 2017). The model has 33 layers, denoted z_k, for $k \in [1,33]$, with layer thickness Δz_k. Resolution is concentrated near the surface; layers are 0.1-m thick from the surface to a depth of 0.6 m, 0.2-m thick from 0.6 to 2 m, and 0.4-m thick from 2 to 10 m.

The thermal evolution in each subsurface layer is a function of vertical heat conduction, latent heat release from meltwater refreezing, and heat advection by meltwater:

$$\rho_s c_s \frac{\partial T}{\partial t} = \frac{\partial}{\partial z}\left(-k_t \frac{\partial T}{\partial z}\right) + \varphi_t + \rho_w c_w q_w \frac{\partial T_w}{\partial z}, \quad (6)$$

where ρ_s and c_s, are the density and specific heat capacity of the subsurface snow or firn, ρ_w and c_w are the density and specific heat capacity of water, and q_w is the vertical rate of meltwater percolation, with units m s^{-1}. The second term on the right-hand-side, φ_t, represents latent heat release from refreezing, with units W m^{-3}, calculated from

$$\varphi_t = \frac{\rho_w L_f \dot{r}}{\Delta z}, \quad (7)$$

where $\dot{r}$ is the refreezing rate (m s^{-1}) and this heat is spread across the layer thickness. The final term in Eq. (6) describes heat advection from meltwater flow, where the temperature derivative $\partial T_w/\partial z$ is with reference to the meltwater, which is assumed to have a temperature of 0°C. Meltwater can percolate downward from layer k to layer k+1, which has temperature $T_{k+1} \leq 0$°C. If the layer is temperate (T_{k+1} = 0°C), there is no heat advection. If it is below 0°C, the firn temperature is adopted in $\partial T_w/\partial z$ and heat advection is calculated from $-\rho_w c_w q_w T_{k+1}/\Delta z$, for $\Delta z = z_k - z_{k+1}$. For the upper layer, the melt rate, $\dot{m}$, is taken as the percolation velocity and Δz is equal to the thickness of the upper layer.

Refreezing occurs when water percolates into a sub-zero layer, accompanied by latent heat release calculated from Eq. (6). Once a layer is temperate, liquid water can be retained within the pore space or it can percolate deeper into the snow or firn. We adopt a simple model for the water flux, $q_w = -k_h \nabla \emptyset$, for hydraulic conductivity k_h and hydraulic potential $\emptyset$ (in m). If conductive energy loss occurs in a subsurface layer where liquid water is present, refreezing takes place before the firn will cool, following Eq. (5). Temperatures cannot drop below 0°C until all of the liquid water is refrozen.

The subsurface model was initiated with the observed snow/firn thermistor temperatures and snow densities at the time of installation for the upper 3.5 m of the snow and firn. Below this, the density and temperature were extrapolated to 10 m depth for the initial conditions. The subsurface model is forced by the net energy and surface melt in the upper layer, calculated from Eqs. (1) and (2).

Surface Energy Balance Results

Figure S2 plots the surface energy balance and modelled melt through summer 2016, along with air temperature and snow depth data fromt the AWS located adjacent to firn pit A. Air temperatures first reached 0°C in mid-May but then cooled again until the main melt season from the second week of June through to late August (Figure S2a).

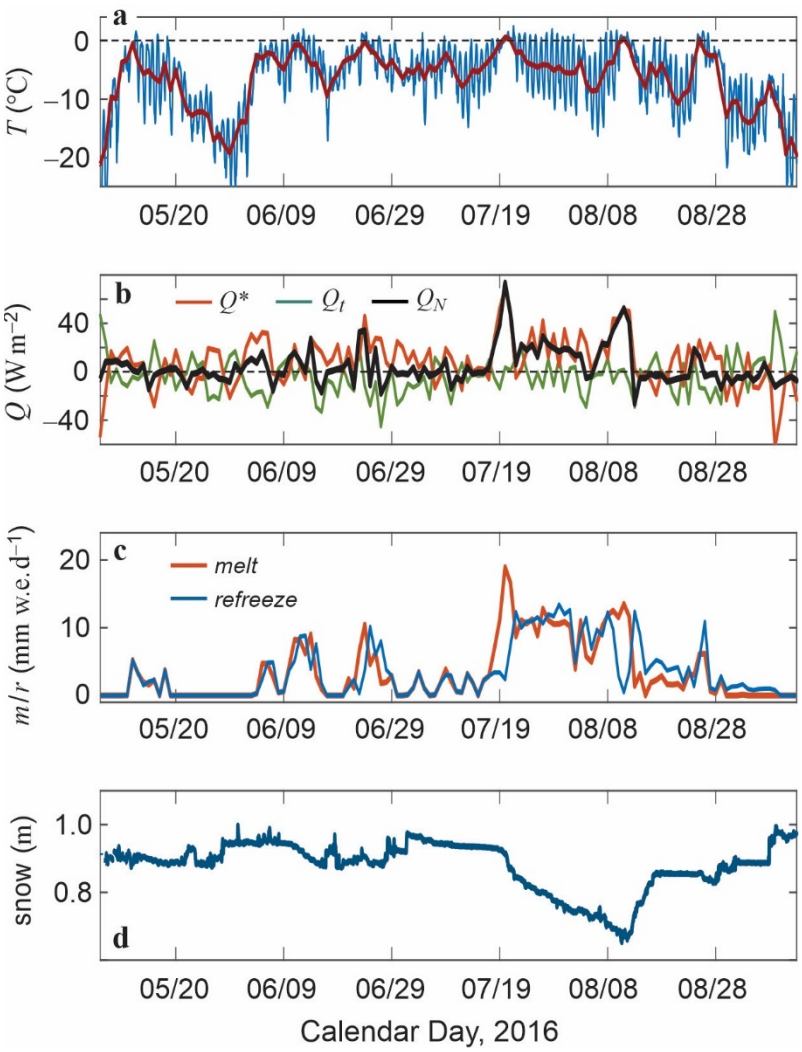

Figure S2. Automatic weather station (AWS) and surface energy balance data from DYE2, May 5 to Sept 11, 2016. (a) Mean daily (red) and 30-minute (blue) air temperature, °C. (b) Mean daily net radiation (Q*), turbulent (Q_t), and net energy (Q_N) fluxes. (c) Modelled daily melt and refreezing, m w.e. (d) Measured snow surface height (m). The initial snow depth was 0.9 m at the time of AWS installation.

Figure S2 plots air temperature, surface energy balance, and modeled melt at the AWS site from May through September, 2016, with results of the surface energy balance and melt model discussed in detail in the Supporting Information. Frequent daily maximum air temperatures above 0°C began in the first week of June and continued through late August, with a return to persistent sub-zero air temperatures after August 26. The main summer melt period was from July 18 to August 9 (Figure S2c). We estimate a total summer melt of 0.51 m w.e., with 0.22 m w.e. of melt from the seasonal snowpack. Meltwater retained near the surface melts and refreezes multiple times in association with diurnal freeze-thaw cycles, such that meltwater is commonly 'recycled', i.e. net energy is used to melt the same snow (and resulting near-surface ice layers and pore water) more than once. Ultrasonic depth gauges installed adjacent to each firn pit recorded a total surface drawdown of ~0.5 m over the summer (Figure S2d), largely offset by several periods of snow accumulation. Snow surface height decreased from its initial value of 0.9 m to a minimum value of 0.66 m on August 9 (Figure S2d), associated with the main period of melting. These data are consistent with the modeled melt, but we note that snow surface lowering also occurs from snow/firn compaction, sublimation, and wind scour. It is difficult to separate these processes in the observational data, so the snow surface height record is not a direct measure of surface melting.

Figure S3 plots the evolution of subsurface snow/firn temperature and dielectric permittivity over the summer melt season at Site A. Liquid water content was consistently detected in association with temperate (0°C) conditions through the melt season, providing a coherent picture of the co-development of thermal and hydrological conditions in the firn. At the time of sensor installation, near-surface firn was in the process of warming from the winter. The snow at 0.3 m depth first warmed to the melting point and showed evidence of liquid water on June 23, roughly two weeks after the initial positive air temperatures. Diurnal cycles of surface melting continued regularly into mid-August (Figure S1), accompanied by firn warming and meltwater infiltration to a depth of between 1.8 and 2.1 m. Sensors at and below 2.1 m depth remained frozen and dry.

Figure S2b plots mean daily energy fluxes at the glacier surface over the summer melt season, including the net radiation, $Q^* = Q_S^{\downarrow}(1-\alpha) + Q_L^{\downarrow} - Q_L^{\uparrow}$, the combined turbulent and conductive fluxes, $Q_t = Q_H + Q_E + Q_C$, and the net energy, Q_N. Mean daily net radiation is near 0 for much of the summer, but is strongly positive on during two periods of heavy cloud cover on July 18-19 and August 9-11, which mark the beginning and end of the main summer melt period. During this period and overall for the summer, net energy is most strongly correlated with net radiation (r = 0.68), compared with a linear correlation coefficient of r = 0.48 for the turbulent fluxes. The mean summer (JJA) net energy was 5.4 W m^{-2}.

Total modelled melt from May through September was calculated to be 0.51 m w.e.

(Figure S2c). Of this, 60% (0.30 m w.e.) melted during the main summer ablation period from July 17 to August 11. All of the melt refroze within the snow and firn, with much of the refreezing occurring in the near-surface (upper 0.1 m). Near-surface ice layers went through successive melt-freeze cycles, such that the actual summer ablation was much less than the total melt. That is, melt energy was used to melt the same snow/ice more than once. The total modelled summer snow melt was 0.22 m w.e.; the remaining 0.29 m w.e. of melting consisted of refrozen ice layers, i.e. recycled meltwater.

This result is consistent with the ultrasonic depth gauge record of snow surface height change, plotted in Figure S2d. These data show several periods of summer snow accumulation, through either snowfall or wind loading, balanced against surface height reductions due to a combination of ablation and densification. The surface height is plotted with reference to the initial (late April) snow thickness of 0.9 m. Cumulative surface height reductions through the summer totaled ~0.5 m, with periods of surface drawdown strongly aligned with the active melt periods. Based on measured snow densities, the 0.22 m w.e. of modelled melt should give a surface drawdown of ~0.54 m, so most of the SR50 signal can be attributed to melting. Compaction immediately following fresh-snow events is visible in the SR50 signal, but densification of deeper snow and firn may have caused sinking of the SR50 pole, masking the surface height signal due to snow/firn compaction.

Thermistor and TDR Data from Firn Pit A

Figure S3 plots the evolution of the summer melt season at firn pit A. Air temperatures first reached 0°C in mid-May but then cooled again until the main melt season, which extended from the second week of June through to mid-August (Figure S3a). Snow surface temperature in Figure S3a is calculated from an inversion of the measured outgoing longwave radiation: $T_s = (Q_L^{\uparrow}/\sigma E_s)^{1/4}$, assuming a surface emissivity E_s of 0.98 (Marks and Dozier, 1992).

At the time of sensor installation, the snow and firn were still frozen and dry, Subsurface temperatures were between −7 and −16°C, decreasing with depth, and initial dielectric permittivity, ε_{b0}, ranged from 1.9 and 2.7 (Table S1). These are all dry-snow values, with some of the difference due to local snow and firn density (Schneebeli et al., 1998); because ice has a greater dielectric permittivity than air, dense snow and firn have higher values of ε_{b0}. The correlation coefficient is 0.55 in our data; hence, other factors such as TDR coupling, grain size and morphology, or potential snow compaction on insertion of the TDR probes also appear to influence ε_{b0}.

Figures S3b and S3c plot subsurface temperatures and dielectric permittivities in the upper 3.7 m of snow and firn at site A through summer 2016. To simplify the plot and focus on the meltwater signal at different depths, dielectric permittivities are plotted as anomalies relative to the initial value for each sensor, $\Delta\varepsilon_b(t) = \varepsilon_b(t) - \varepsilon_{b0}$. Changes in ε_b

over the summer are associated with either densification (a gradual increase in ε_b) or wetting/drying of the snow, which produces abrupt increases/decreases in ε_b.

Data in Figure S3 were quality-controlled to reject unphysical values and gap-fill any missing data through linear interpolation. The thermistor and automatic weather station data were complete, with no errant values, but TDR data gaps were frequent, giving rejection rates of 32 to 81% for the individual sensors at site A. TDR data were also much more complete at site B: from 74 to 99% for individual sensors, with an average of 94%. We are unsure why the TDR records from this site have less data gaps than at Site A. It is possible that electromagnetic signals at Site A were impacted by the adjacent AWS (which reported to the same datalogger) or the upwards-looking snow radar that was installed ~5 m from the TDR installation. The TDR sensors give a noisy signal compared to the thermistors, but the combined records provide a reliable account of the coupled thermal and hydrological evolution in the near-surface firn over summer 2016.

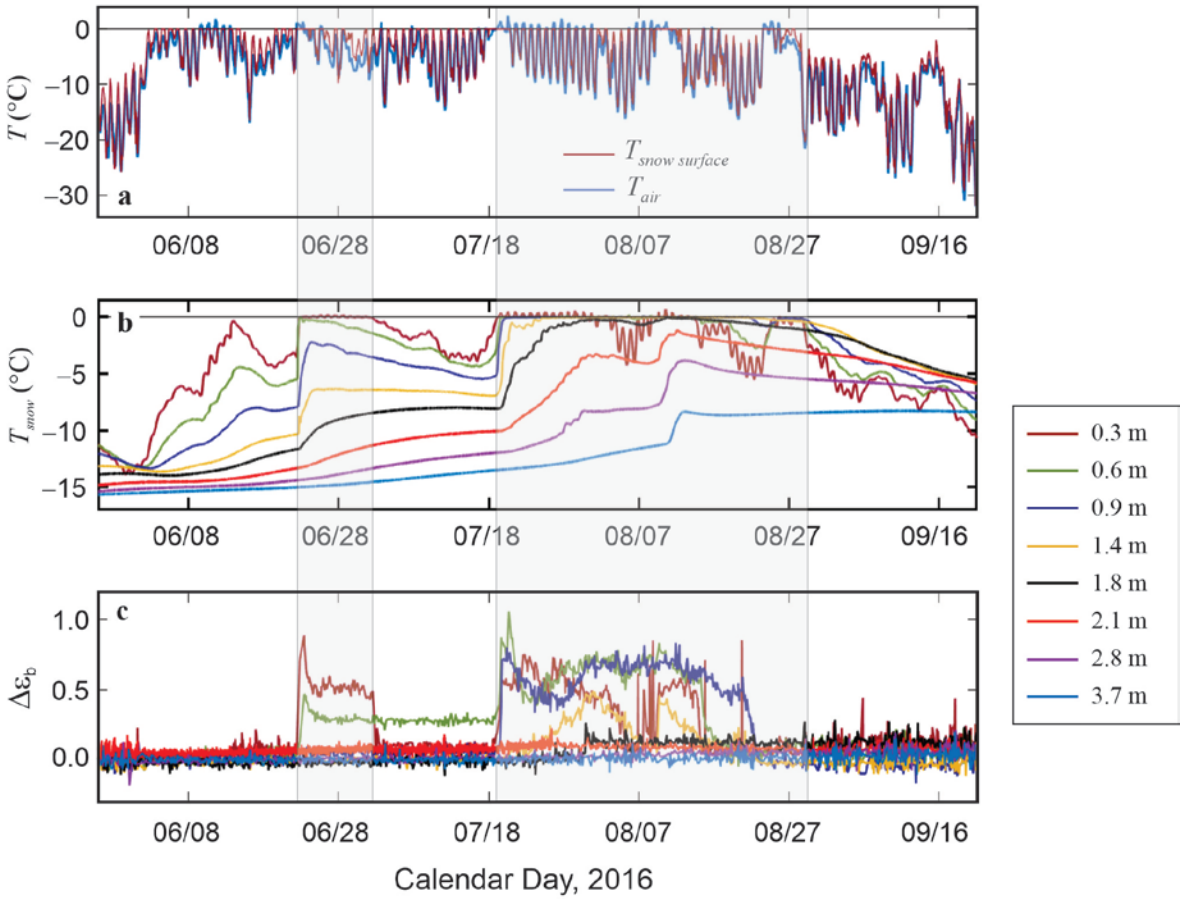

Figure S3. Measured (a) air and snow surface temperatures, (b) snow temperatures, and (c) dielectric permittivity anomalies in firn pit A, May 27 to Sept 21, 2016. Shaded areas indicate periods with temperate snowpack conditions, based on the thermistor records.

Modelled Subsurface Energy Fluxes

The firn model, driven by the AWS data, facilitates a detailed examination of the subsurface energy fluxes and coupled hydrological and thermodynamic processes. Model details and sensitivities will be discussed in a followup manuscript, but Figure S4 plots the results of a simulation that gives a good fit to the observed firn temperature and TDR data in summer 2016. Figure S4c shows the simulated temperature evolution in the upper 4 m of the snow and firn, capturing the observed rapid warming events and the penetration of the melting/wetting front to approximately 2 m depth in August.

The warming events are associated with meltwater infiltration and latent heat release. Where meltwater enters a sub-zero snow layer with temperature T_k, there is an associated heat advection, calculated from:

$$E_{adv} = -\rho_w c_w q_w T_k \,, \tag{8}$$

with units J m^{-2}. There can similarly be an advection of energy out of the layer if meltwater is percolating to a greater depth. The latent heat release from refreezing is calculated from:

$$E_{ref} = \rho_w L_f \dot{r} \,, \tag{8}$$

also with units J m^{-2}. Integrated values of these two energy fluxes are plotted in Figures S4a and S4b for the summer melt season. Figure S4a shows total daily energy released by each process, integrated over the depth of the firn, and Figure S4b plots the energy release as a function of depth, integrated over the melt season. Latent heat release dominates the subsurface energy transport associated with meltwater infiltration, totalling 141 MJ m^{-2} over the summer (JJA) compared with 0.9 MJ m^{-2} for the heat transport from meltwater advection.

Also shown in Figure S4a are the total daily surface energy fluxes associated with melting and warming the snowpack. These are calculated from the amount of positive net energy that is directed to each. The total summer (JJA) energy flux directed to melt equals 141 MJ m^{-2}, identical to the latent heat release from refreezing as 100% of the meltwater refreezes locally. The total summer (JJA) net energy directed to warming of the surface layer equals 76 MJ m^{-2}; much of this energy is conducted downwards into the snow and firn. Latent heat release is the primary source of energy for subsurface warming (64.9%), but net energy at the surface that is directed to warming of the snow and firn is also significant (34.7%). Advective heat transfer by meltwater percolation accounted for the remaining 0.4%. In the months of May and September, warming energy exceeds melt energy (62 vs. 6 MJ m^{-2}), but there is little melt in these months; firn warming is concentrated in the main summer melt season in the months of July and August (Figure S4c), when meltwater infiltration plays a critical role in transporting latent

energy to depth.. The net energy directed to warming in May is, however, important to priming the snow and firn for the melt season.

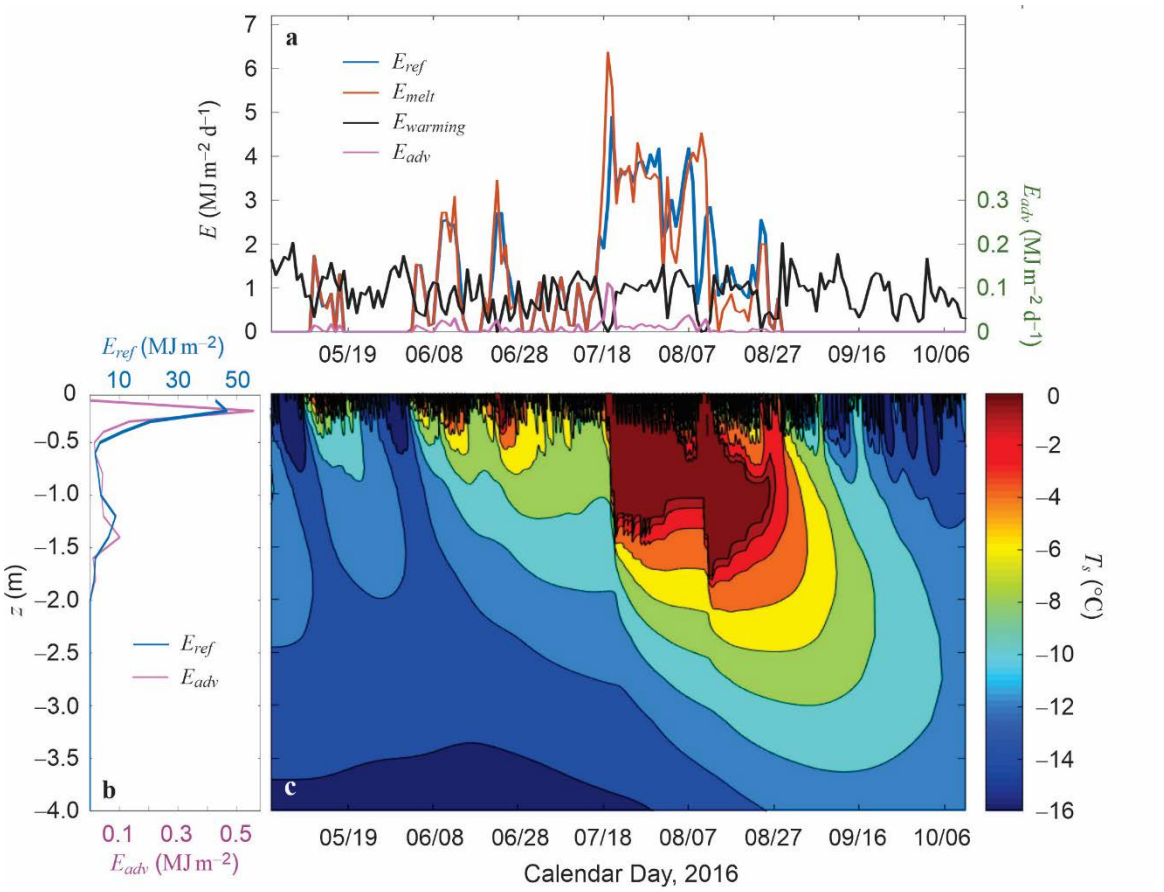

Figure S4. Modelled surface and subsurface energy fluxes and temperatures in the upper 4 m of snow and firn from May 1 to October 10, 2016. (a) Daily surface energy (MJ m^{-2} d^{-1}) directed to melting and warming the snow/firn, along with the subsurface energy release due to refreezing (*ref*) and meltwater advection (*adv*). (b) Depth profile of subsurface energy release due to latent heat of refreezing and meltwater advection, integrated over the full summer melt season. Note the different scales. (c) Subsurface temperature evolution in the upper 4 m, with the 0°C isotherm (wetting front) reaching a maximum depth of 1.9 m in the second week of August.

Supplementary References

Brock, B.W., Willis I. C., & Sharp, M. J. (2006). Measurement and parameterisation of aerodynamic roughness length variations at Haut Glacier D'Arolla, Switzerland. *Journal of Glaciology*, *52* (177), 281–297

Cuffey, K. M., & Paterson, W. S. B. (2010). *The Physics of Glaciers*, 4th Ed.

Ebrahimi, S., & Marshall, S. J. (2016). Surface energy balance sensitivity to meteorological variability on Haig Glacier, Canadian Rocky Mountains, *The Cryosphere*, *10*, 2799–2819, https://doi.org/10.5194/tc-10-2799-2016.

Marks, D., & Dozier, J. (1992). Climate and energy exchange at the snow surface in the Alpine region of the Sierra Nevada: 2. Snow cover energy balance. *Water Resources Research*, *28*, 3043–3054, https://doi.org/10.1029/92WR01483.

Samimi, S., & Marshall, S. J. (2017). Diurnal cycles of meltwater percolation, refreezing, and drainage in the supraglacial snowpack of Haig glacier, Canadian Rocky Mountains. *Frontiers in Earth Science*, *5*, 6, https://doi.org/10.3389/feart.2017.00006.

Schneebeli, M., Coléou, C., Touvier, F. & Lesaffre, B. (1998). Measurement of density and wetness in snow using time-domain reflectometry. *Annals of Glaciol*ogy, *26*, 69-72, https://doi.org/10.3189/*1998AoG26*-1-69-72.

Data Set S1. The dataset for this study is being archived at the University of Calgary data repository, and is also available on request from the authors. AWS, TDR, and thermistor data were written to a Campbell Scientific CR1000 datalogger and the raw (ascii) output from the datalogger is imported to an Excel spreadsheet. Data have been quality-controlled through the elimination of any non-physical values (e.g., -99999); these are replaced with NaN or blanks in the dataset. In the publication figures, linear interpolation was used in MATLAB to gap-fill missing TDR data. The thermistor and AWS data were complete. Ultrasonic depth gauge (SR50A) data were filtered to remove non-physical values and erroneous data associated with spurious reflections from blowing snow.